Catalytic and redox properties of bimetallic Cu–Ni systems combined with CeO$_2$ or Gd-doped CeO$_2$ for methane oxidation and decomposition

A. Hornés [a], P. Bera [a,1], M. Fernández-García [a,b], A. Guerrero-Ruiz [b,c], A. Martínez-Arias [a,b,*]

[a] Instituto de Catálisis y Petroleoquímica (CSIC), C/ Marie Curie 2, Campus de Cantoblanco, 28049 Madrid, Spain
[b] Unidad Asociada UNED-ICP(CSIC), Grupo de Diseño y Aplicación de Catalizadores Heterogéneos, Madrid, Spain
[c] Departamento de Química Inorgánica y Química Técnica, Facultad de Ciencias, UNED, C/ Senda del Rey 9, 28040 Madrid, Spain

ARTICLE INFO

ABSTRACT

Two catalysts combining Cu–Ni with CeO$_2$ and Gd-doped CeO$_2$, respectively, are comparatively examined with respect to redox and catalytic properties towards interaction with CH$_4$. For this, catalysts in oxidised starting states are explored by means of CH$_4$-TPR tests up to 973 K. Characterization of initial and final states of the catalysts is accomplished by means of XRD, Raman spectroscopy and EXAFS while carbon deposits formed during interaction with CH$_4$ are examined by TPO, Raman spectroscopy and SEM–EDX. Oxygen handling characteristics of the catalysts are examined by means of oxygen isotopic exchange experiments. In turn, redox changes produced during the course of CH$_4$-TPR tests are explored by operando-XANES. Methane oxidation or decomposition processes are observed as a function of redox state of the catalysts and sites involved in each of the processes are identified on the basis of the multitechnique approach employed.

© 2011 Elsevier B.V. All rights reserved.

1. Introduction

Solid oxide fuel cells (SOFC) are galvanic devices which are most interesting from environmental and energetic points of view due to their high efficiency for conversion from chemical to electrical energy and their high versatility towards employment of various types of fuels [1]. Classical systems of this type involve the employment of thin YSZ electrolytes with an anode typically based on Ni–YSZ cermets and can attain an energetic efficiency close to 70% operating at relatively high temperature (1073–1273 K) with hydrocarbon reforming mixtures as fuel [1–3]. This efficiency can be theoretically increased by employing direct hydrocarbon oxidation conditions instead of fuel mixtures resulting from reforming [4]. However, the classical anode of nickel could easily be deactivated under those conditions as a consequence of the formation of carbonaceous deposits due to the relatively good activity of nickel

for hydrocarbon cracking [4–7]. Different alternatives were developed in this respect to overcome such deactivation effects. Murray et al. successfully operated a cell on dry methane by employing a nickel-containing ceria-based anode at relatively low reaction temperature (923 K) [5]. In turn, such ceria-containing anode could in principle be compatible with electrolytes able to operate at intermediate temperatures (773–973 K) like gadolinium-doped ceria (CGO) [1].

However, nickel anodes are prone to become rapidly deactivated by deposited carbon under direct hydrocarbon oxidation conditions [4,6–9]. A more versatile alternative in this respect was developed by Gorte, Vohs and co-workers and consisted in employing anodes including mixtures between copper and cerium oxide [4,6,9–13]. Such configuration has demonstrated to be able to employ a large diversity of hydrocarbon fuels (methane or longer chain ones and even aromatics) under direct oxidation conditions and displaying a reasonable stability [4,6,11]. However, although it could in principle perform well at intermediate temperatures, the copper anode can present several limitations related to its relatively low melting temperature, which can make the fabrication of Cu cermets difficult and affect the anode stability when operating at high temperature [4,14], as well as to its poor performance for hydrocarbon activation [4,8]. An interesting alternative in this sense consists in employing bi- or multi-metallic anode

* Corresponding author at: Instituto de Catálisis y Petroleoquímica (CSIC), C/ Marie Curie 2, Campus de Cantoblanco, 28049 Madrid, Spain. Tel.: +34 915 85 49 40; fax: +34 915 85 47 60.
   E-mail address: amartinez@icp.csic.es (A. Martínez-Arias).
[1] Present address: Surface Engineering Division, National Aerospace Laboratories, Bangalore 560017, India.

formulations [4,8,15–17]. Among them, specific formulations of bimetallic Cu–Ni anodes can apparently display promising properties for the process [17–19].

Additionally, bimetallic Cu–Ni catalysts are also most interesting for hydrogen production through methane decomposition [20]. In particular, it has been shown that bimetallic Cu–Ni formulations can present advantages with respect to monometallic Ni ones, basically as a consequence of limiting deactivating effects by carbon deposition, for which parameters like metal or alloy particle size, reaction temperature or type of support employed appear most relevant [20–29].

In this context, the present work explores the properties of bimetallic Cu–Ni configurations for methane oxidation by oxygen from the solid catalyst and subsequent methane decomposition taking place after reduction of the catalysts, employing CeO_2 or Gd-doped CeO_2 as supports. Comparison between the two systems allows the determination of the influence of the addition of Gd to CeO_2, which may be beneficial for this class of reaction through enhanced oxygen transport and thus increased gasification of the carbonaceous deposits produced [30–33]. For this purpose, catalysts synthesized by a microemulsion method (which have shown excellent characteristics as SOFC anodes for direct methane oxidation both in terms of electrochemical performance and stability [34,35]) have been examined structurally by XRD, S_{BET} and Raman spectroscopy while oxygen transport properties have been analysed by oxygen isotopic exchange measurement; redox/catalytic properties have been explored by means of TPR tests under dry methane in a catalytic reactor as well as by operando-XANES; in turn, structural/chemical analysis of the post-reaction specimens has been carried out by XRD, EXAFS, SEM and Raman spectroscopy as well as by TPO. The results show the evolution of catalyst components from oxidised to reduced states upon interaction with CH_4 which leads to formation of Cu–Ni alloys; their catalytic properties, which are shown to depend on the presence of Gd dopant in the catalyst formulation, are examined as a function of redox changes taking place in the catalysts. It must be also noted that previous contributions of the group have analysed similar catalysts formulations towards interaction with CH_4 in previous articles [31,33]. However, in those cases, the catalysts were calcined at 1223 K as final preparation step instead of 973 K employed here. Employment of a lower calcination temperature allows an important enhancement of the catalytic properties of these systems as a general consequence of the lower particle size and higher specific surface area which are achieved for the latter. In any case, employment of the latter calcination temperature is also motivated by development of SOFC preparation methods based on wet impregnation which allow decreasing the calcination temperature applied to the anode down to ca. 750 K, while 973 K is a reasonable temperature for the operation of this type of fuel cells [4]. In turn, it may be noted that the analysis of redox properties of the catalysts subjected to interaction with CH_4, which constitutes the central part of this contribution, is carried out here to a much deeper level than in those mentioned previous works [31,33], mainly as a consequence of employment of operando-XANES spectroscopy and isotopic exchange techniques.

2. Experimental

2.1. Catalyst preparation

Catalysts combining Cu–Ni with CeO_2 or $Ce_{0.9}Gd_{0.1}O_{2-x}$ were prepared by coprecipitation within reverse microemulsions. For this purpose, two reverse microemulsions, of similar characteristics concerning the volumes employed of organic (n-heptane) and aqueous phases as well as of surfactant (Triton X-100) and co-surfactant (1-hexanol), were prepared; details of the method can be found elsewhere [36]. The first one contained in its aqueous phase the dissolved (nitrate) salts of Ce, Gd, Cu or Ni while the second one contained in its aqueous phase a dissolved base (tetramethyl ammonium hydroxide or TMAH) which is employed as precipitating agent. Mixing both microemulsions causes precipitation of the cations and, after separation by centrifugation and decanting, the resulting solid is rinsed with methanol and dried for 24 h at 373 K. The resulting material is then calcined under air at 973 K during 2 h, employing heating ramps of 2 K min^{-1}. Samples with total metal loading of 40 wt.% (with 1/1 Cu/Ni atomic ratio) have been prepared. Chemical analysis of the samples by ICP-AES demonstrated quantitative precipitation in all samples, the actual contents of any component being the same (within experimental error) as the nominal values employed. The samples will be denoted hereafter as CuNi-C and CuNi-CG depending on whether the support material is CeO_2 or $Ce_{0.9}Gd_{0.1}O_{2-x}$, respectively.

2.2. Techniques

Specific surface area (S_{BET}) determination was made from curves of adsorption/desorption of N_2 at 77 K performed over the samples outgassed at 413 K using a Micromeritics ASAP 2100 equipment. Powder XRD patterns of the samples were recorded on a Seifert XRD 3000P diffractometer using nickel-filtered Cu K$_\alpha$ radiation operating at 40 kV and 40 mA, using a 0.02° step size and 2 s counting time per point. Scherrer equation, employing most intense diffraction peak in each case, has been used to determine crystal sizes; in the case of fluorite phase detected in the samples (vide infra) this approximation is considered to underestimate crystal size in only about 5% for the range of sizes obtained (according to comparison with estimations from Williamson–Hall plots in some case), being therefore a reasonable approach. Raman spectra were collected using a Horiba Jobin-Ybon iHR320 spectrometer. The samples were excited with the He:Ne red laser line (632.8 nm); the spectral resolution was ca. 3 cm^{-1} and spectrum acquisition consisted of 5 accumulations with a total of ca. 10 min acquisition time. Scanning electron microscopy/energy dispersive X-ray (SEM–EDX) analysis was made with a Hitachi S-2500 microscope; four different points were explored by EDX in each sample.

Temperature programmed reduction (TPR) tests under diluted methane (5% CH_4/He) – CH_4-TPR tests – were done in a quartz flow microreactor filled with about 500 mg of sample and employing 150 mL min^{-1} total flow. Heating ramps of 10 K min^{-1} from 303 to 973 K, maintaining finally this temperature until products stabilized (about 2 h) under the reactant mixture, were used. Pretreatment was in any case done under diluted O_2 (20% in He) flow at 773 K. Gases evolving from the reactor were analysed with a Pfeiffer Omnistar quadrupolar mass spectrometer.

Oxygen isotopic exchange experiments were carried out with ca. 20 mg of sample held into a recirculating quartz reactor coupled to a grease-free standard vacuum system [37]. The gas phase was analysed with an on-line quadrupole spectrometer (SRS RGA 200) connected to the reactor through a metering leak valve. Calcined samples (200 Torr of $^{16}O_2$ at 773 K for 30 min) were subjected to outgassing at room temperature and to a subsequent circulation of ca. 50 Torr of $^{18}O_2$ using a 10 K min^{-1} ramp, with continuous analysis of gaseous products. The same equipment was employed to carry out temperature programmed oxidation (TPO) tests with $^{18}O_2$ of samples subjected to CH_4-TPR tests in the XANES cell (vide infra) after thorough room temperature outgassing.

X-ray absorption near edge structure (XANES) experiments at the Cu and Ni K-edges and also at the Ce L$_{III}$-edges were performed at station BM-25 (Spline) of the ESRF (Grenoble, France) synchrotron. A Si(1 1 1) double-crystal monochromator was used in conjunction with a rejection mirror to minimise the harmonic content of the beam. Transmission experiments were carried out
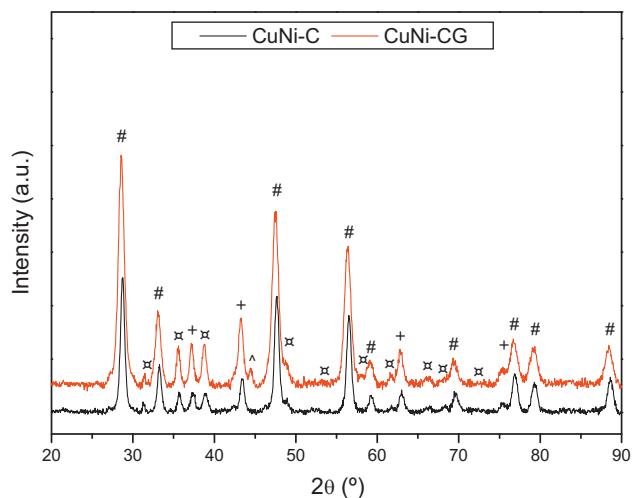
Fig. 1. X-ray diffractograms of the indicated samples. Symbols: (#) fluorite, ($\bowtie$) CuO, (+) NiO, (^) Ni (this latter belonging to sample holder).
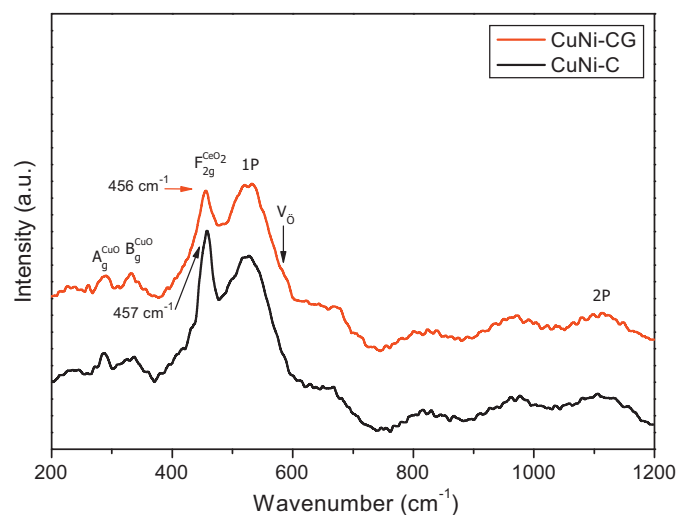

Fig. 2. Raman spectra of the indicated samples.

using noble gas- or N_2/O_2-filled ionisation chambers as detector. The energy scale was simultaneously calibrated by measuring a Cu foil, a Ni foil or a pure CeO_2 disc (used as references) employing a third ionisation chamber. Self-supporting discs made by mixing the sample with inert silica were employed (absorbance 1.0–2.0) and placed in a controlled-atmosphere cell (Specac 5850) for *in situ* treatment. The spectrum of a Ce^{3+} reference ($CeAlO_3$ compound) was taken from a previous contribution [38]. Gas analyses were performed on line by means of a Balzers mass spectrometer. The samples were pretreated under diluted oxygen (20% in He) at 773 K and XANES spectra were taken in the presence of a diluted CH_4 (5% in He) flow during a $5\,K\,min^{-1}$ ramp up to maximum temperature attained by the experimental equipment (typically below 973 K).

3. Results and discussion

3.1. Characterization of the initial calcined catalysts

Specific surface area measurements yield values of S_{BET} = 14 and $18\,m^2\,g^{-1}$ for CuNi-C and CuNi-CG, respectively. Fig. 1 displays X-ray diffractograms of the initial samples calcined at 973 K. Peaks due to the fluorite phase of CeO_2 or Gd-doped CeO_2 are detected in the diffractograms. The lattice parameter determined for this phase in CuNi-C, Table 1, appears slightly higher than that expected for pure CeO_2 (a = 5.410 Å). This can be due to the presence of residual amounts of Ce^{3+} cations and/or to some substitutional incorporation of copper or nickel cations into the fluorite lattice as a consequence of associated oxygen vacancies formation [39,40], as will be complemented below by Raman spectroscopy. In turn, the slight expansion of this phase in CuNi-CG in comparison with CuNi-C must be attributed to Gd^{3+} incorporation to the fluorite lattice [41]. The presence of peaks due to tenorite CuO, in agreement also with lattice parameters estimated from them (Table 1), is also observed for both samples. Concerning the Ni-containing phase, peaks detected are similar to those expected for cubic NiO although the lattice parameter detected in this case (Table 1) appears slightly larger than that observed for such phase (a = 4.177 Å [42]). A possibility in this sense, as will be discussed below on the basis of Raman spectroscopy results, is that such lattice expansion is due to formation of cubic Cu–Ni mixed oxide and the estimated lattice parameter would be in agreement with a composition close to $Ni_{0.85}Cu_{0.15}O$ (Table 1). Table 1 collects also crystal sizes estimated from corresponding diffraction peak widths. As observed, doping with Gd^{3+} produces an appreciable decrease of fluorite crystal size

while it does not apparently affect strongly to sizes of copper or nickel oxides crystals.

Raman spectra of the initial samples calcined at 973 K are shown in Fig. 2. In agreement with XRD results, Raman spectra display peaks due to CuO at ca. 290, 335 and $625\,cm^{-1}$ (A_g + $2B_g$ modes, respectively) [43], fluorite CeO_2 or Gd-doped CeO_2 at ca. $460\,cm^{-1}$ (F_{2g} mode) [41], and nickel- or nickel–copper oxide (most intense bands expected to appear at ca. 550 and $1100\,cm^{-1}$ corresponding to one and two phonon excitations, respectively; broad bands at ca. 820 and $980\,cm^{-1}$ could also correspond to two phonons excitations in this type of oxide [44]). Fluorite F_{2g} mode appears slightly red-shifted with respect to that expected for pure CeO_2 [41]. This can be caused either by the presence of Ce^{3+} or by incorporation of Cu^{2+} or Ni^{2+} cations in the fluorite structure [39,40,45]. However, a stronger shift would be expected in the case when Cu^{2+} or Ni^{2+} cations are introduced to a significant degree (considering in any case a solubility limit of about 10% in the fluorite structure) [39,40,46,47], suggesting that no important incorporation of such cations is produced in this case. Concerning the nickel-containing oxide phase, the ratio between intensities of main 1P and 2P bands at ca. 550 and $1100\,cm^{-1}$, respectively, provides qualitative measurement of the amount of defects in the corresponding oxide cubic phase [44]. In our case, the relatively high intensity of mentioned 1P band suggests a significant amount of defects must be present in such oxide phase, which can be related to the presence of copper in it according to XRD estimations discussed above.

3.2. Oxygen handling properties of the initial calcined catalysts

Fig. 3 shows the evolution of the three isotopically labelled oxygen molecules following tests of temperature programmed oxygen isotopic exchange upon exposure to $^{18}O_2$. Both simple and multiple heteroexchange [48], giving rise to $^{18}O^{16}O$ and $^{16}O_2$, respectively, are observed for the two catalysts. Differences between them are related to the lower temperature and higher oxygen exchange rate (defined as in [49]) observed for CuNi-CG (Fig. 3), as well as the higher relative contribution of multiple heteroexchange for this sample. This latter typically indicates predominance of associated defects at the sample surface as it occurs in the presence of doped ceria samples [49,50]. Also the obtained results show that the overall amount of oxygen exchanged by the CuNi-CG sample is almost double that of CuNi-C (1.20×10^{-4} mol vs. 6.46×10^{-5} mol). This in turn indicates that almost double the amount of oxygen from the bulk is employed in the exchange in the former compared to the

Table 1
Summary of main physicochemical parameters [lattice parameters (a, b, c, β) and crystal size (d)] extracted for indicated phases from XRD data.

Sample	CeO$_2$ or Gd-doped CeO$_2$		Ni$_{0.85}$Cu$_{0.15}$O		CuO				
	a (Å)	d (nm)	a (Å)	d (nm)	a (Å)	b (Å)	c (Å)	β (°)	d (nm)
CuNi-C	5.415	13.3	4.185	14.3	4.694	3.422	5.141	99.32	13.8
CuNi-CG	5.417	9.4	4.186	13.5	4.690	3.420	5.144	99.30	14.1
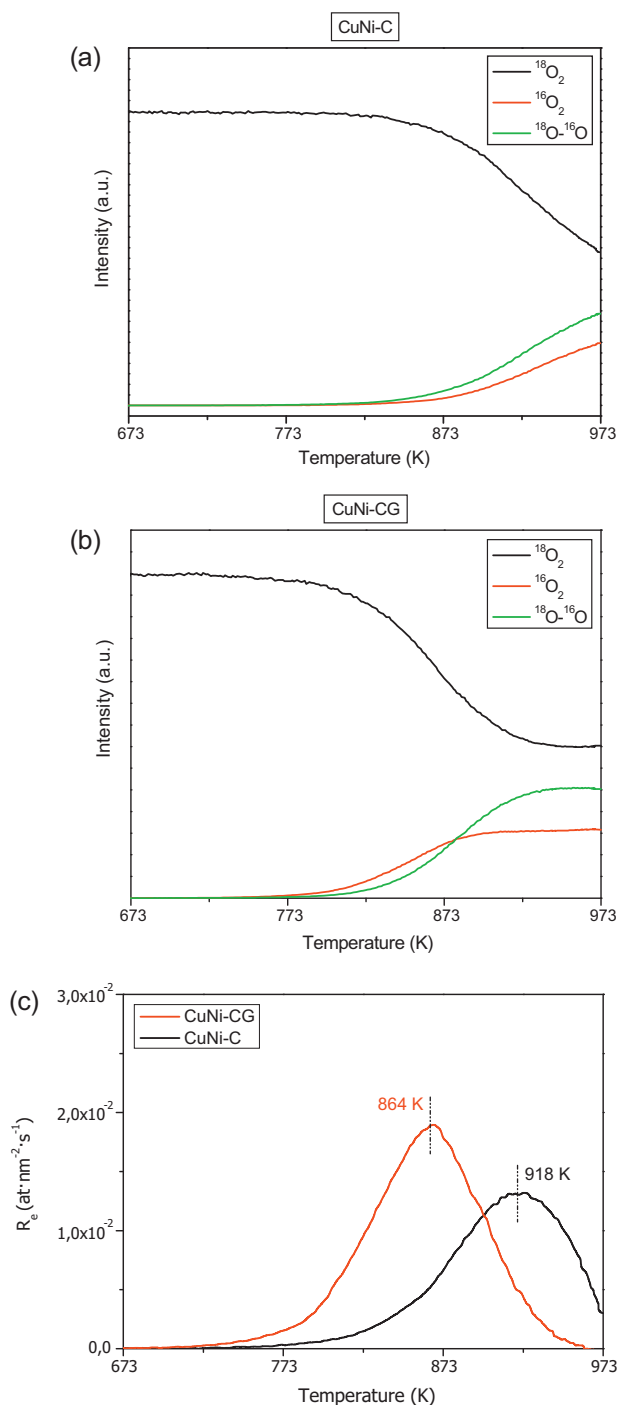
Fig. 3. Evolution of the three molecular oxygen isotopologues upon exposure of the initial calcined samples CuNi-C (a) and CuNi-CG (b) to $^{18}O_2$. (c) Calculated oxygen exchange rate for the indicated samples during the course of the oxygen isotopic exchange tests shown in (a) and (b).

latter (assuming all surface oxygen – approximately corresponding to 4.23×10^{-6} and 3.24×10^{-6} mol – is exchanged in the two cases, around 1.16×10^{-4} and 6.14×10^{-5} mol of bulk oxygen are exchanged by CuNi-CG and CuNi-C, respectively).

3.3. Catalytic/redox properties: CH$_4$-TPR tests

A first set of tests was performed by employing the conventional tubular reactor; the results obtained being displayed in Fig. 4. For both catalysts, products resulting from full CH$_4$ oxidation (i.e. CO$_2$ + H$_2$O) appear first. However, onset of such reaction is produced at appreciably lower temperature for CuNi-CG (673 K) than for CuNi-C (773 K). In any of the two catalysts, upon increasing reaction temperature, following such initial process and after apparent stabilization of CO$_2$ and H$_2$O concentrations, a sharp increase in these products is apparent (i.e. also related to full CH$_4$ oxidation reaction). Slightly after this sharp full oxidation process, it is observed a significant increase in H$_2$ production, which becomes maximised at the highest reaction temperature employed (973 K)
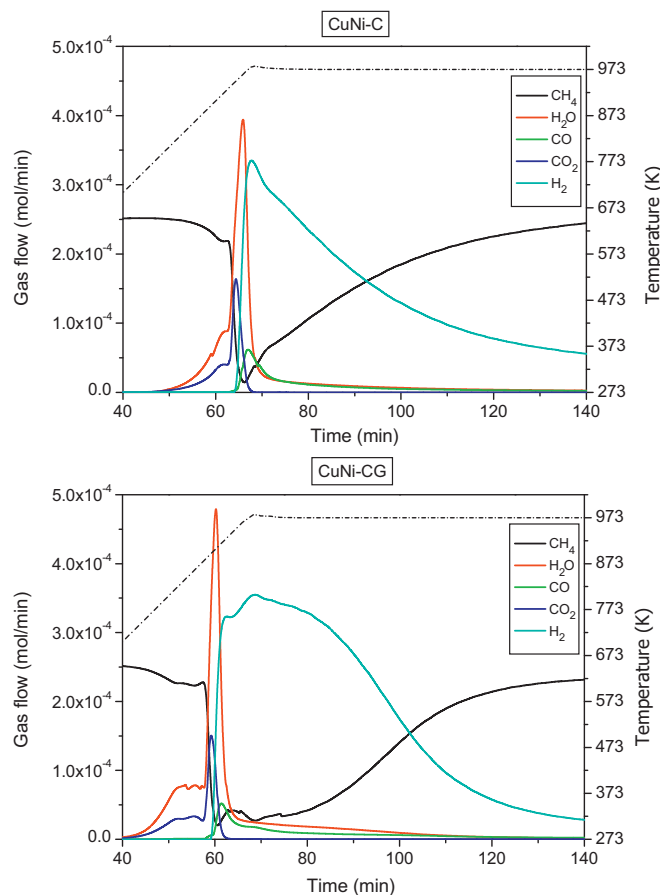
Fig. 4. Evolution of the indicated gases during CH$_4$-TPR tests over CuNi-C (top) and CuNi-CG (bottom). Note the temperature evolution is presented as dashed line with corresponding scale at the right.
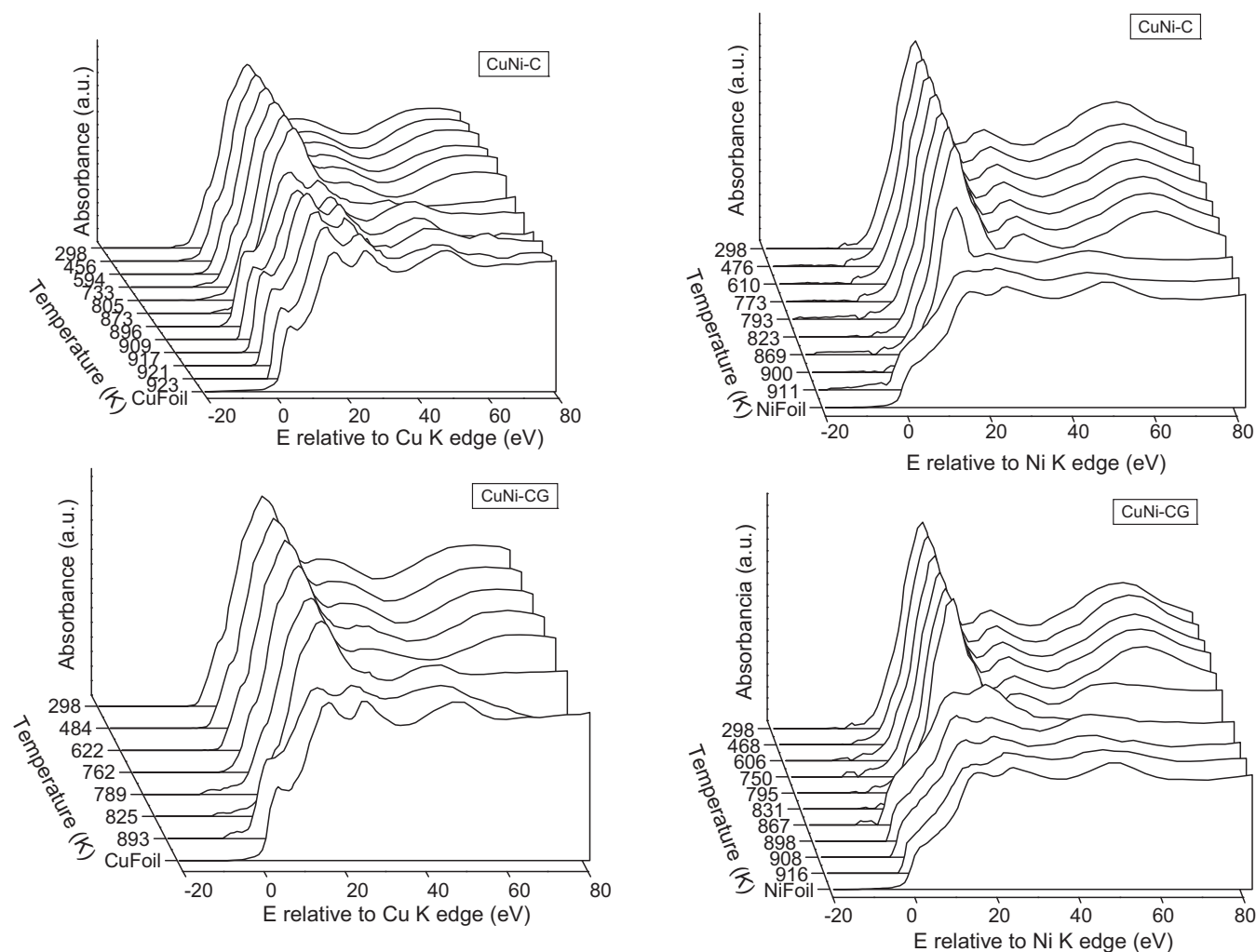
Fig. 5. XANES spectra in the Cu (left) and Ni (right) K-edges recorded during the course of CH_4-TPR tests over CuNi-C (top) and CuNi-CG samples (bottom).

along with a small CO production, which reveals the presence of partial oxidation processes over the catalysts. Both CO and CO_2 productions gradually extinguish more or less rapidly, revealing in turn that the availability of oxygen from the catalysts becomes gradually lost. In any case, CH_4 decomposition strongly prevails after aforementioned sharp CO_2 production peak, according to the high H_2 concentration detected. CH_4 decomposition must be accompanied by carbon formation which gradually deactivates the catalysts, remaining only a residual decomposition activity, somewhat higher for the CuNi-C system, at the end of the test. Nevertheless, overall CH_4 conversion during the whole test is higher for CuNi-CG (23.2%) than for CuNi-C (17.1%), thus demonstrating a beneficial effect of Gd dopant in this sense. This affects both to oxidation processes (either total or partial ones and on the basis of total oxygen extracted from the catalyst: 4.35×10^{-3} and 5.01×10^{-3} mol for CuNi-C and CuNi-CG, respectively, which in turn corresponds approximately to 0.88×10^{-3} and 1.33×10^{-3} mol of oxygen extracted from the bulk) and methane decomposition (selectivity towards H_2 and solid carbon formation, the latter based on carbon material balance, is of 84.7 and 82.9% for CuNi-C, and 85.9 and 86.4% for CuNi-CG, respectively).

Analysis of the gas evolutions produced during CH_4-TPR tests can provide hints on the type of entities involved in the oxidation or decomposition processes. Thus, the fact that only full oxidation products CO_2 and H_2O are generated at first stages of CH_4 interaction with the catalysts suggests it must be mainly CuO reduction

which is involved in the process. This follows from the fact that the activity of metallic copper for methane decomposition is rather poor and previous observations in the literature showing the reduction with CH_4 of pure CuO basically involves generation of full oxidation products [51,52]. Then, the sharp increase of CO_2 and H_2O production (along with the fact that it is immediately followed by formation of mainly H_2 and some CO), must be essentially related to reduction of the $Ni_{0.85}Cu_{0.15}O$ component leading to generation of metallic Ni responsible for methane partial oxidation or decomposition products, in accordance to expected reactivity for such component [51,53]. In any case, for the sake of the clarity of the redox processes taking place in the catalysts upon interaction with CH_4, the samples were examined under CH_4-TPR conditions while simultaneously recording XANES spectra. Fig. 5 displays the spectra recorded for the two samples at the Cu and Ni K edges. Initial spectra are in both cases analogous to those found for Cu^{2+} in CuO or Ni^{2+} in oxidic environments (like NiO or $Ni_{0.85}Cu_{0.15}O$), respectively, in agreement with XRD or Raman spectroscopy results (Figs. 1 and 2) [47,54]. They evolve with increasing reaction temperature towards final states which are close to those found in pure metallic Cu and Ni, in agreement with comparison with reference Cu and Ni foils spectra, respectively, as confirmed below by EXAFS and XRD. Transition from the oxidised to the fully reduced state is very fast, which makes very difficult stabilization and characterization of possible intermediate states formed; i.e. it is most likely that chemical changes are produced in the course of recording of any determinate spectrum
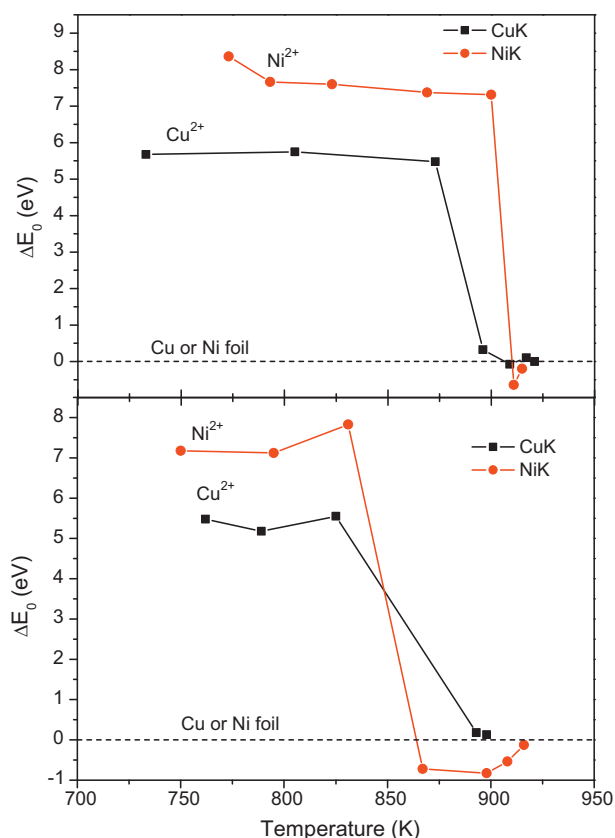
Fig. 6. Evolution of Cu or Ni K absorption edge position (arbitrarily taken at the energy of the first maximum in the first derivative spectrum, see main text) as a function of temperature during CH$_4$-TPR runs over CuNi-C (top) and CuNi-CG (bottom) samples. Note the edge shift is normalized with respect to the position of mentioned first maximum in Cu or Ni metallic foils used as reference during spectra recording.

Fig. 7. Evolution of reactant and product gases during CH$_4$-TPR runs in the XANES cell for CuNi-C (top) and CuNi-CG (bottom).

during such transition stages. Under such conditions, it is not feasible to perform a full analysis of the chemical states of Cu or Ni contributing to every spectrum. Nevertheless, significant insight into redox changes can be achieved by analysing the shift of the absorption edge position during the course of the CH$_4$-TPR runs. In this sense, the absorption edge can be (more or less arbitrarily) considered to lie at first maximum in the first derivative spectra, taking also into account that this provides a reasonable measurement of the valence state in each case [55,56]. This is shown in Fig. 6 while gases evolutions during the course of corresponding CH$_4$-TPR runs are shown in Fig. 7. According to this, copper and nickel reduction occurs practically in a simultaneous way under these experimental conditions, being both in principle responsible of production of full oxidation products CO$_2$ and H$_2$O. A subtle difference between the two samples in this sense appears related to the slight delay in nickel reduction with respect to copper detected for CuNi-C (Fig. 6). In any case, as discussed above, metallic nickel thus generated must be mainly responsible of CH$_4$ decomposition activity. As was apparent with the tubular catalytic reactor (Fig. 4), a significant shift to lower temperature is observed in the reaction onset when Gd is present in the fluorite phase (Fig. 7), thus confirming its promoting role for the process. A question remains nevertheless as to whether oxygen species from the fluorite phase intervene to some extent on CH$_4$ oxidation processes. In this sense, XANES spectra in the Ce L$_{III}$ edge show that cerium begins to be reduced from Ce^{4+} to Ce^{3+} concomitantly with nickel and copper although in a more gradual and limited way. Thus, as shown in Fig. 8, according to comparison with reference spectra, cerium reduction starts above 863 and 825 K for CuNi-C and CuNi-CG, respectively. A
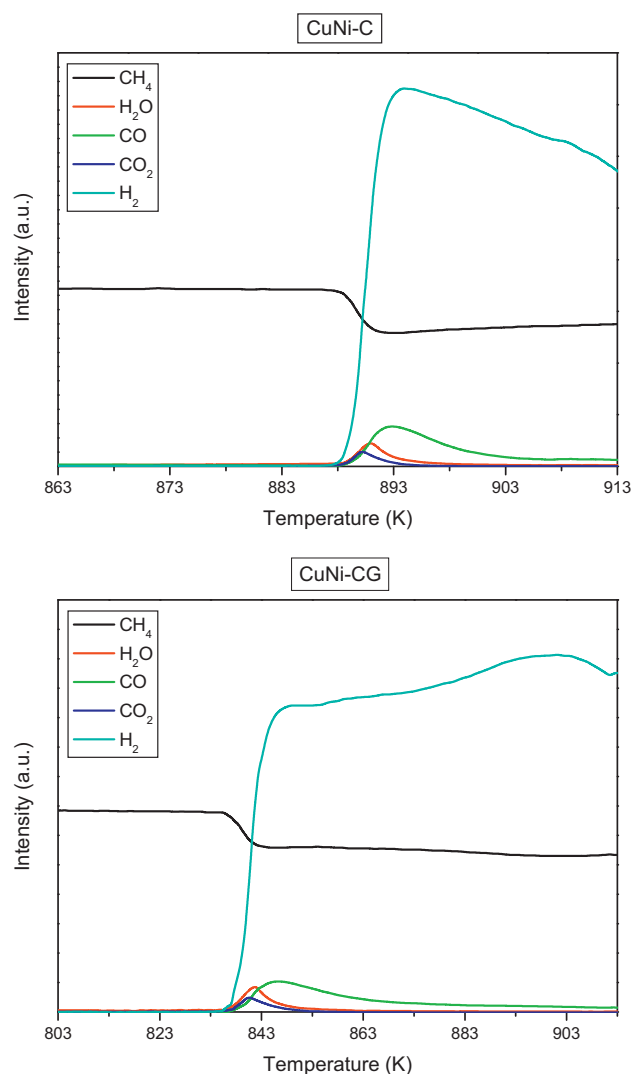
limited degree of cerium reduction is apparently produced above such temperature (starting between 863 and 907 K) for CuNi-C. In contrast, reduction of cerium in CuNi-CG occurs between 825 and 861 K. The spectrum recorded at this latter temperature had to be stopped because the disc became broken with progress of the reaction under the particular conditions employed to record these spectra and only for this particular sample (the experiment was repeated twice with the same unfortunate result); in any case, the shape of such incomplete spectrum suggests, in agreement with oxygen consumption estimations done above for the experiments with the tubular reactor (Fig. 4), a higher cerium reduction degree is achieved for this sample which could in turn favour the important brittleness observed for this sample. In turn, the gradual nature of the reduction of this component (as observed for CuNi-C) supports attribution of partial CH$_4$ oxidation giving rise to formation of residual CO amounts (at least at temperatures above which full reduction of copper and nickel oxides is accomplished, ca. 890 and 910 K for CuNi-CG and CuNi-C, respectively, considering results in Figs. 7 and 8) to it, in agreement with expected activity of pure CeO$_2$ towards *syngas* production [57]. In any case, reduction level achieved by this component appears considerably lower than that detected for copper or nickel oxide components.

Thus, to summarize this part, CH$_4$ oxidation is produced as a consequence of mainly CuO and Ni$_{0.85}$Cu$_{0.15}$O reduction, which
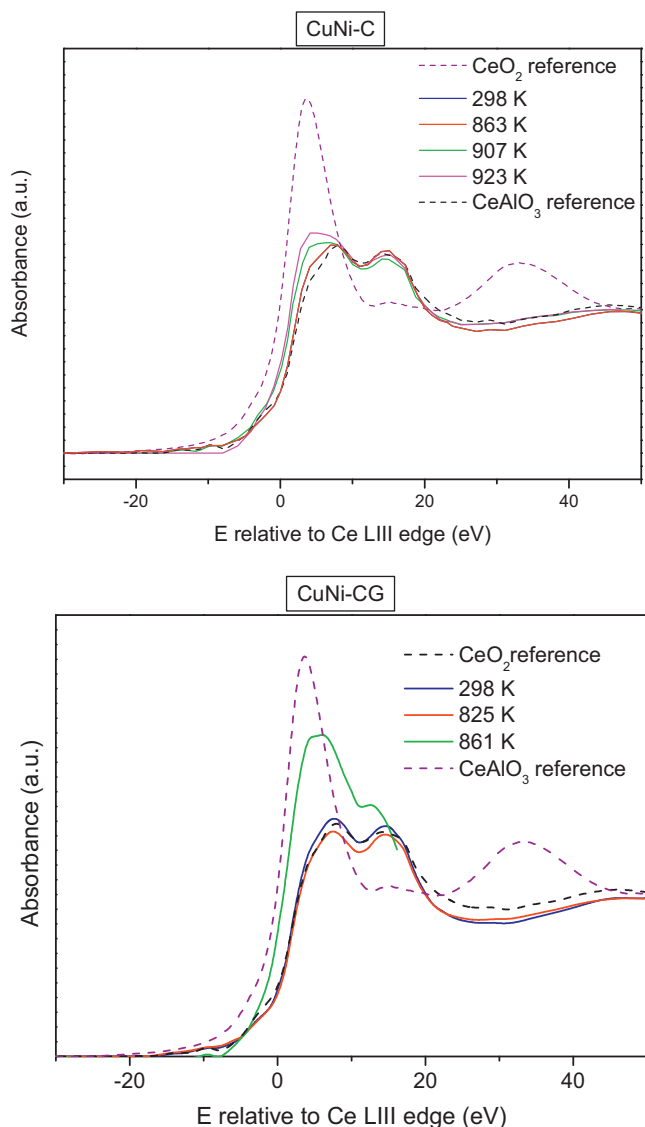
Fig. 8. XANES spectra in the Ce L$_{III}$ edge recorded during CH$_4$-TPR tests over CuNi-C (top) and CuNi-CG (bottom) at the indicated temperatures and compared with those of Ce^{4+} and Ce^{3+} reference compounds (see text for details).

occurs practically simultaneously, although this latter can depend on the experimental conditions employed (in this sense, according to results in Fig. 4, as discussed above, CuO could likely be reduced at slightly lower temperature than Ni$_{0.85}$Cu$_{0.15}$O; such differential reduction appears however less pronounced during experiments performed with the XANES cell, particularly for CuNi-CG), while a small concomitant reduction of cerium in the fluorite phase is also produced. The presence of Gd in the fluorite phase appreciably shifts oxidation reaction onset to lower temperature. In any of the two catalysts, the three oxide components become practically reduced (the fluorite component at a considerably lower extent) simultaneously, thus showing that they basically act as a whole. It appears reasonable in this sense that the higher oxygen mobility demonstrated for CuNi-CG (Fig. 3) facilitates CH$_4$ activation and reaction. In turn, it appears feasible, given the concomitant reduction observed, that the oxidation of CH$_4$ starts at interfacial sites between the metal oxides and the fluorite phase, which are in principle most reducible sites for this type of oxides combinations [58], being immediately propagated towards most reducible sites in the metal oxides and, to a more limited and gradual extent, towards

sites on the rare earth oxide fluorite phase [58]. On the other hand, differences between the two catalysts in terms of CH$_4$ decomposition activity appear generally smaller than those detected for the full oxidation reaction. This suggests CH$_4$ decomposition activity may essentially depend on the properties of metallic nickel active sites which must be fairly similar for both catalysts, as will be discussed below. Nevertheless, as pointed out above, differences in the experimental conditions employed in each case (tubular vs. XANES cell reactors) can result in subtle differences in terms of redox/catalytic properties. Thus, the higher overall CH$_4$ decomposition activity of CuNi-CG and the slightly higher CH$_4$ decomposition conversion observed at the end of the test for CuNi-C in the experiments with the tubular reactor (Fig. 4) suggests subtle differences in the characteristics of CuNi alloys formed in each case, *vide infra*. In this sense, small differences in the extent of surface enrichment in nickel, alloy particle size or local environment of nickel active sites in them as well as respective levels of deactivation by carbon deposits could explain such differences [20,21]. Related to this, previous reports on similar catalysts, in terms of component amounts and preparation method employed, although in a more sintered state as a consequence of employment of higher final calcination temperature (1173 K) during sample preconditioning, also displayed catalytic differences as a function of the presence of Gd; these were related to the characteristics of the Cu–Ni alloy formed in each case, in turn related to differences in the reduction temperature of copper and nickel oxide components [31,33,34].

3.4. Characterization of the catalysts after CH$_4$-TPR tests

Fig. 9 displays the X-ray diffractograms observed for the samples after CH$_4$-TPR tests in the XANES cell. In addition to peaks from CeO$_2$ or Gd-doped CeO$_2$ appearing at the same positions than for initial samples (Fig. 1) (note that the fully oxidised state observed for these phases must be a consequence of reoxidation upon exposure to atmospheric air), peaks due to CuNi alloy are detected for the two catalysts with Cu:Ni atomic composition close to 1:1 although slightly more enriched in Cu for CuNi-C (lattice parameter of 3.587 and 3.581 Å for CuNi-C and CuNi-CG, respectively) [59], in agreement also with achievement of full reduction in the two components evidenced by XANES results (Fig. 6). The slight enrichment in Cu for the alloy formed in CuNi-C is in agreement with a slightly higher delay in nickel reduction in it, according to XANES results in Fig. 6, favouring formation of a core slightly more enriched in Cu in it; this in turn suggests a somewhat higher surface enrichment in Ni for the alloy formed in this sample. Indeed, such compositional heterogeneity appears also reflected by the apparent asymmetry observed in the XRD peaks of the alloy for CuNi-C; it is however difficult to ascertain whether this reflects a more or less continuous compositional gradient from a Ni-enriched surface to a Cu-enriched bulk or the presence of two or more crystalline phases as responsible of such effect. In any case, formation of the CuNi alloy has also been confirmed by EXAFS for CuNi-C. As shown in Fig. 10, CuNi-C displays two intense signals at ca. 2.2 and 4.5 Å for both Cu K and Ni K EXAFS spectra. While practically no difference between the two pure metals or between these and the alloy are observed, as expected, in first shell contribution at ca. 2.2 Å, the apparent coincidence observed in third coordination sphere contribution at about 4.5 Å in the R-space spectra of the CuNi-C sample, which strongly contrasts with those of the pure metals references, clearly evidences the alloy presence in that sample. On the other hand, it can be noted that the fact that all of the copper and nickel become reduced during the CH$_4$-TPR run is evidenced by the absence of a contribution at ca. 1.8 Å, expected for either Cu–O or Ni–O in the spectra of corresponding oxides [39,40], in the spectra of CuNi-C.
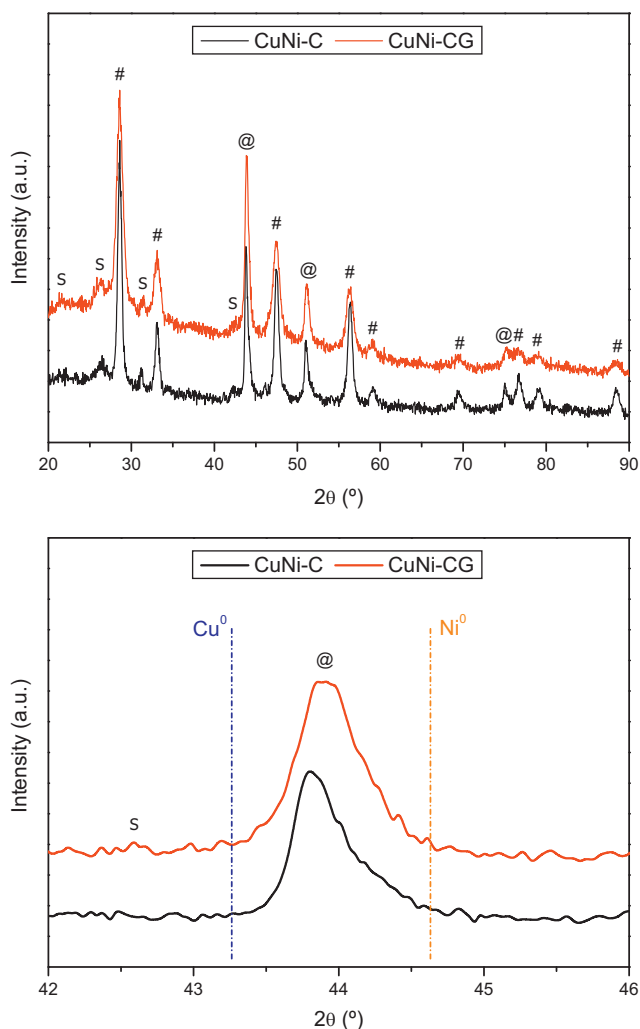
Fig. 9. X-ray diffractograms of the indicated samples after CH_4-TPR runs in the XANES cell up to 913 K and cooling under inert gas flow (and exposure to air at room temperature). The bottom graph shows the expanded region corresponding to most intense peak of the Cu–Ni alloy along with positions expected for the pure metals. Symbols: (#) Fluorite CeO_2 or Gd-doped CeO_2; (@) Cu–Ni alloy; (S) SiO_2 (from silica employed to prepare discs, see Section 2).
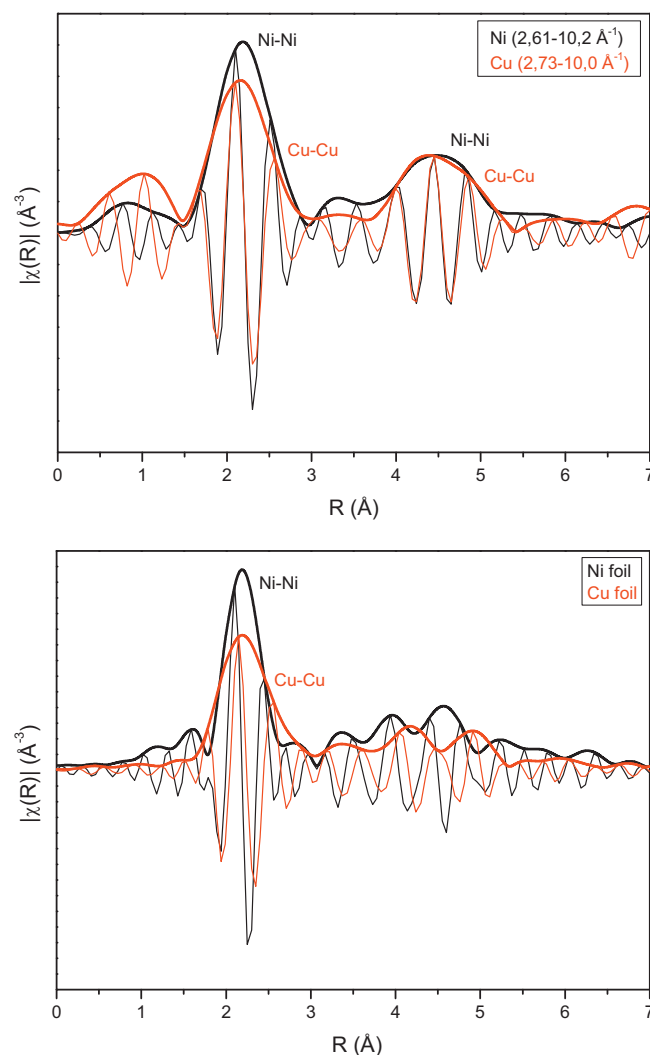
Fig. 10. Pseudo-radial distribution functions extracted from EXAFS spectra in Cu and Ni K regions of CuNi-C after CH_4-TPR test and cooling to room temperature (top). The same analysis done on Cu and Ni foils references is displayed for comparative purpose (bottom).

3.5. Characterization of carbon deposits formed during CH_4-TPR tests

SEM–EDX analysis of the samples after CH_4-TPR tests in the XANES cell show the formation of considerable amounts of filamentous carbon deposits on both catalysts (Fig. 11) formed, as discussed above, as a consequence of CH_4 decomposition process taking place over the Cu–Ni alloy. On the basis of EDX analysis, fairly similar amounts of carbon are formed in the two catalysts while catalyst composition is in agreement with ICP-AES chemical analysis of the initial samples.

The fact that about similar amounts of carbon deposits are formed on the two catalysts is confirmed by TPO tests. As described in Section 2, these were conducted employing isotopically labelled $^{18}O_2$ as reactant, aiming to differentiate between possible contributions of CO_2 formed as a consequence of carbon deposits oxidation from those resulting from decomposition of carbonates, taking into account that this type of samples are, mainly as a consequence of ceria basic character, prone to become carbonated upon exposure to atmospheric air. Results obtained are displayed in Fig. 12. In principle, no CO_2 from carbonate decomposition is obtained on the basis of the absence of observation of the isotopologue $C^{16}O_2$. In this

sense, since it can be assumed that oxygen can be also exchanged by carbonate species prior to their decomposition, it must be noted that observation of $C^{18}O^{16}O$ evolving at fairly similar temperature than $C^{18}O_2$ suggests that the two isotopologues are originated by the same process (carbon oxidation) and observation of the former can be explained by the fact that some of the $^{18}O_2$ can be partially exchanged with ^{16}O from the ceria or Gd-doped ceria component, according to Fig. 3, previously or simultaneously to CO_2 formation. Fairly similar overall amounts of CO_2 are formed for the two catalysts, thus evidencing that similar amounts of carbon deposits are formed. It may be noted that no significant differences are detected in the gasification temperatures for the two catalysts, thus evidencing basically similar nature of the carbon deposits formed. It is not possible however to employ gasification temperatures observed during this test to get hints on the nature of such deposits upon comparison with classical TPO experiments done with more or less ideal reactors in flowing conditions, taking into account the experimental conditions here used (static system in which CO_2 is not eliminated, thus possibly shifting carbon combustion to higher temperature with respect to classical TPO tests).

In order to get insight into the nature of carbon deposits, the samples after CH_4-TPR tests were examined by Raman
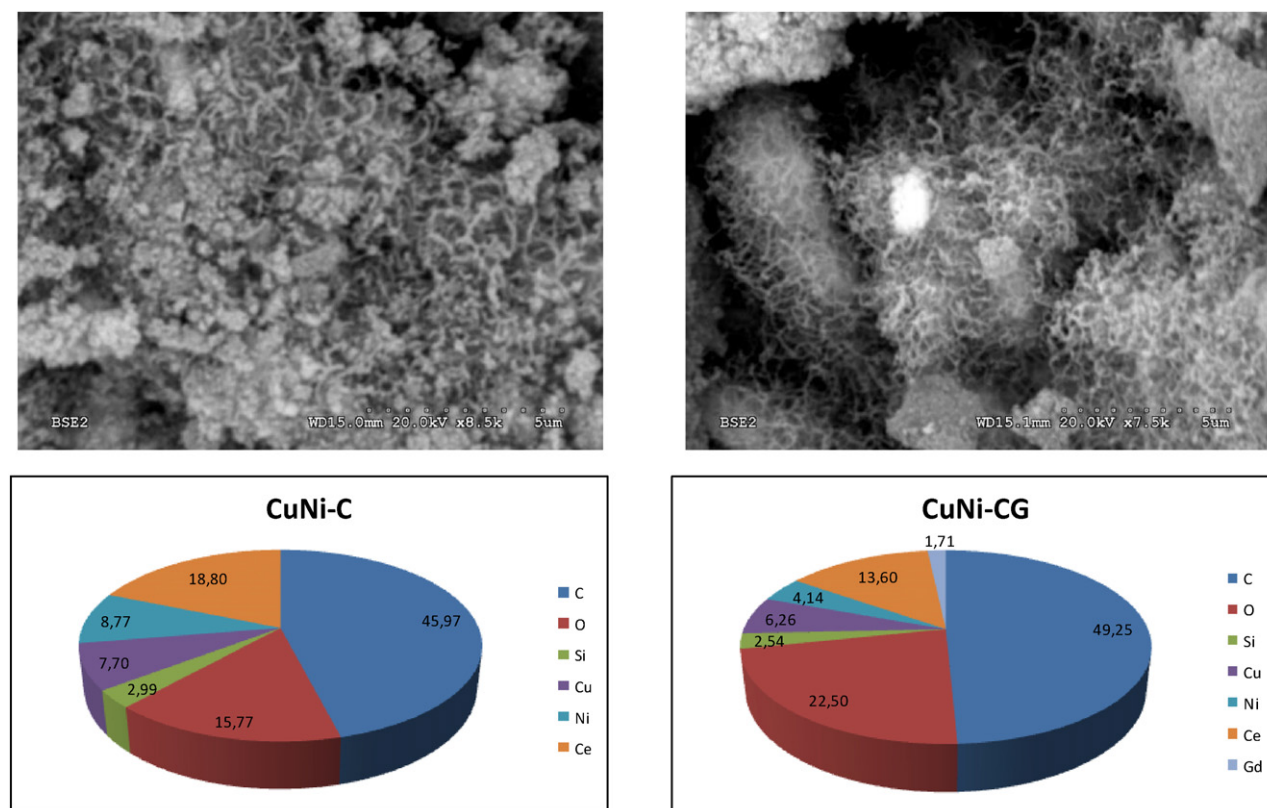
Fig. 11. SEM images of CuNi-C (left) and CuNi-CG (right) after CH_4-TPR tests in the XANES cell and representative EDX analyses.

spectroscopy. Fig. 13 displays representative spectra for the two samples. Concerning carbon deposits, the spectra display two main bands D and G (using typical notation [60]), the latter with a blue shoulder D1, and two less intense bands G1 and D2. As well known [60,61], the relative intensity of these types of band provides hints on the nature of the carbon deposits. Thus, in principle bands G and G1 are inherent to graphitic structures, the latter typically becoming split into two bands when highly crystalline graphite is present. The degree of crystallinity of such graphitic structures in principle decreases upon increasing the intensity of band D while band D2 is typical for imperfect graphitic structures or disordered carbons.

On this basis, in addition to other possible factors like position of the G band or its FWHM, insight into the degree of crystallinity of the carbon deposits can be achieved by analysing the intensity ratio between bands D and G. This yields values of $I_D/I_G = 1.0$–1.5 and 1.2–1.8 (range related to performing measurements at different sample positions, thus revealing some heterogeneity in carbon deposits nature and distribution) for CuNi-C and CuNi-CG, respectively, which indicate a relatively low crystallinity of the carbon deposits (in agreement with their absence from X-ray diffractograms in Fig. 9, considering also they constitute a major portion of these samples, according to SEM–EDX, Fig. 11), in agreement also with the absence of splitting in band G1.
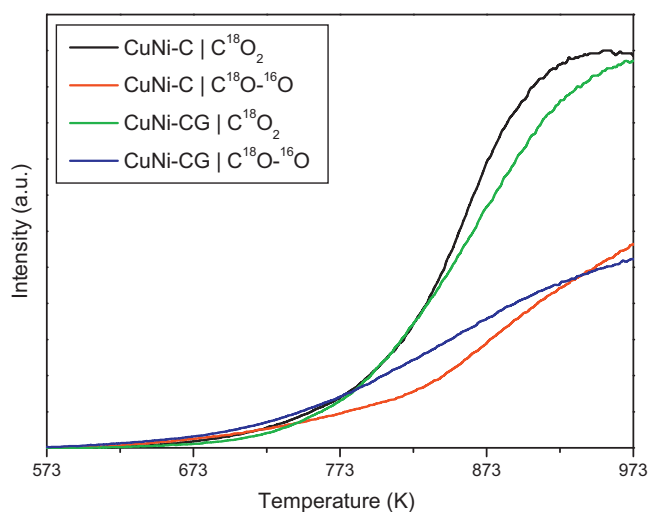

Fig. 12. Evolution of indicated CO_2 isotopologues during TPO tests performed over indicated samples after CH_4-TPR tests in the XANES cell.
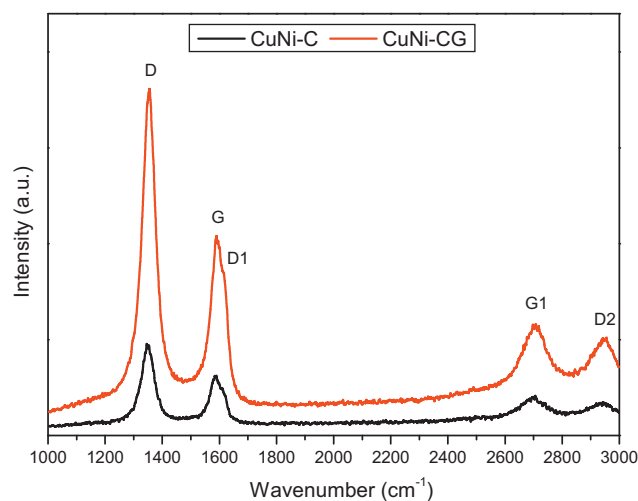

Fig. 13. Raman spectra of the indicated samples after CH_4-TPR runs in the XANES cell. See text for identification of the symbols.

4. Summary and conclusions

Two catalysts combining Cu–Ni with CeO_2 or Gd-doped CeO_2, respectively, are examined with respect to their interaction with CH_4 by means of CH_4-TPR tests. Evolution of the redox state of the catalysts, starting from oxidised states, is explored during the course of such tests by XANES with simultaneous analysis of the products evolving, which allows identification of the species involved in CH_4 oxidation or decomposition processes observed. On this basis, full CH_4 oxidation giving rise to CO_2 and H_2O is basically related to reduction of CuO or $Ni_{0.85}Cu_{0.15}O$ components present in the initial oxidised catalysts, which become fully reduced during the CH_4-TPR test in a very fast way. A considerably more limited and gradual reduction of the fluorite component (either CeO_2 or Gd-doped CeO_2, higher for the latter) occurs during the reaction which is identified as being responsible for the production of the remaining CO (likely within a process of *syngas* formation, in accordance with known activity of such phase for this reaction). In any case, the three components become reduced practically in a concomitant way (with details depending on experimental conditions employed) which gives rise to generation of Cu–Ni (close to 1:1 atomic) alloys responsible of CH_4 decomposition activity. In any case, the catalysts become gradually deactivated as a consequence of formation of amorphous filamentous carbon deposits, according to characterization by Raman spectroscopy and SEM–EDX. An important promoting effect of Gd on CH_4 oxidation by catalyst oxygen species is revealed and related to the enhancement in oxygen transport properties, examined by oxygen isotopic exchange, produced in the presence of such dopant in the fluorite component. In contrast, relatively small differences are detected in CH_4 decomposition activity which is related to the similarities observed in the characteristics of the Cu–Ni alloys, acting as active centres for such reaction, formed in each case.

Acknowledgements

References

[1] B.C.H. Steele, A. Heinzel, Nature 414 (2001) 345.
[2] B.C.H. Steele, J. Mater. Sci. 36 (2001) 1053.
[3] J.M. Ralph, A.C. Schoeler, M. Krumpelt, J. Mater. Sci. 36 (2001) 1161.
[4] S. McIntosh, R.J. Gorte, Chem. Rev. 104 (2004) 4845.
[5] E.P. Murray, T. Tsai, S.A. Barnett, Nature 400 (1999) 649.
[6] S. Park, R.J. Gorte, J.M. Vohs, Appl. Catal. A 200 (2000) 55.
[7] A.-L. Sauvet, J. Fouletier, J. Power Sources 101 (2001) 259.
[8] N.M. Galea, D. Knapp, T. Ziegler, J. Catal. 247 (2007) 20.
[9] R.J. Gorte, J.M. Vohs, J. Catal. 216 (2003) 477.
[10] S. Park, R. Craciun, J.M. Vohs, R.J. Gorte, J. Electrochem. Soc. 146 (1999) 3603.
[11] S. Park, J.M. Vohs, R.J. Gorte, Nature 404 (2000) 265.
[12] H. Kim, S. Park, J.M. Vohs, R.J. Gorte, J. Electrochem. Soc. 148 (2001) A693.
[13] R.J. Gorte, H. Kim, J.M. Vohs, J. Power Sources 106 (2002) 10.
[14] S. Jung, C. Lu, H. He, K. Ahn, R.J. Gorte, J.M. Vohs, J. Power Sources 154 (2006) 42.
[15] C. Sun, U. Stimming, J. Power Sources 171 (2007) 247.
[16] Z. Xie, W. Zhu, B. Zhu, C. Xia, Electrochim. Acta 51 (2006) 3052.
[17] S.I. Lee, J.M. Vohs, R.J. Gorte, J. Electrochem. Soc. 151 (2004) A1319.
[18] E.W. Park, H. Moon, M. Park, S.H. Hyun, Int. J. Hydrogen Energy 34 (2009) 5537.
[19] D. La Rosa, A. Sin, M. Lo Faro, G. Monforte, V. Antonucci, A.S. Aricò, J. Power Sources 193 (2009) 160.
[20] H.F. Abbas, W.M.A. Daud Wan, Int. J. Hydrogen Energy 35 (2010) 1160.
[21] H. Wang, R.T.K. Baker, J. Phys. Chem. B 108 (2004) 20273.
[22] A. Monzón, N. Latorre, T. Ubieto, C. Royo, E. Romeo, J.I. Villacampa, L. Dussault, J.C. Dupin, C. Guimon, M. Montioux, Catal. Today 116 (2006) 264.
[23] D. Li, J. Chen, Y. Li, Int. J. Hydrogen Energy 34 (2009) 299.
[24] A.F. Cunha, J.J.M. Orfão, J.L. Figueiredo, Int. J. Hydrogen Energy 34 (2009) 4763.
[25] I. Suelves, M.J. Lázaro, R. Moliner, Y. Echegoyen, J.M. Palacios, Catal. Today 116 (2006) 271.
[26] T.V. Reshetenko, L.B. Avdeeva, Z.R. Ismagilov, A.L. Chuvilin, V.A. Ushakov, Appl. Catal. A 247 (2003) 51.
[27] J. Ashok, P.S. Reddy, G. Raju, M. Subrahmanyam, A. Venugopal, Energy Fuels 23 (2009) 5.
[28] M.J. Lázaro, Y. Echegoyen, I. Suelves, J.M. Palacios, R. Moliner, Appl. Catal. A 329 (2007) 22.
[29] Y. Echegoyen, I. Suelves, M.J. Lázaro, M.L. Sanjuán, R. Moliner, Appl. Catal. A 333 (2007) 229.
[30] M. Fernández-García, A. Martínez-Arias, J.C. Hanson, J.A. Rodriguez, Chem. Rev. 104 (2004) 4063.
[31] A. Hornés, D. Gamarra, G. Munuera, J.C. Conesa, A. Martínez-Arias, J. Power Sources 169 (2007) 9.
[32] T.-J. Huang, C.-H. Wang, Chem. Eng. J. 132 (2007) 97.
[33] A. Hornés, D. Gamarra, G. Munuera, A. Fuerte, R.X. Valenzuela, M.J. Escudero, L. Daza, J.C. Conesa, P. Bera, A. Martínez-Arias, J. Power Sources 192 (2009) 70.
[34] A. Hornés, PhD Thesis, Universidad Autónoma de Madrid, 2010.
[35] A. Hornés, M.J. Escudero, A. Martínez-Arias, in preparation.
[36] A. Martínez-Arias, M. Fernández-García, V. Ballesteros, L.N. Salamanca, J.C. Conesa, C. Otero, J. Soria, Langmuir 15 (1999) 4796.
[37] A. Guerrero-Ruiz, P. Ferreira-Aparicio, M.B. Bachiller-Baeza, I. Rodríguez-Ramos, Catal. Today 46 (1998) 99.
[38] A. Martínez-Arias, M. Fernández-García, L.N. Salamanca, R.X. Valenzuela, J.C. Conesa, J. Soria, J. Phys. Chem. B 104 (2000) 4038.
[39] X. Wang, J.A. Rodriguez, J.C. Hanson, D. Gamarra, A. Martínez-Arias, M. Fernández-García, J. Phys. Chem. B 109 (2005) 19595.
[40] L. Barrio, A. Kubacka, G. Zhou, M. Estrella, A. Martínez-Arias, J.C. Hanson, M. Fernández-García, J.A. Rodriguez, J. Phys. Chem. C 114 (2010) 12689.
[41] J.R. McBride, K.C. Hass, B.D. Poindexter, W.H. Weber, J. Appl. Phys. 76 (1994) 2435.
[42] Y. Shimomura, M. Kojima, S. Saito, J. Phys. Soc. Jpn. 11 (1956) 1136.
[43] J.F. Xu, W. Ji, Z.X. Shen, W.S. Li, S.H. Tang, X.R. Ye, D.Z. Jia, X.Q. Xin, J. Raman Spectrosc. 30 (1999) 413.
[44] N. Mironova-Ulmane, A. Kuzmin, I. Steins, J. Grabis, I. Sildos, M. Pärs, J. Phys. Conf. Ser. 93 (2007) 12039.
[45] J.E. Spanier, R.D. Robinson, F. Zhang, S.-W. Chan, I.P. Herman, Phys. Rev. B 64 (2001) 245407.
[46] W. Shan, W. Shen, C. Li, Chem. Mater. 15 (2003) 4761.
[47] D. Gamarra, G. Munuera, A.B. Hungría, M. Fernández-García, J.C. Conesa, P.A. Midgley, X.Q. Wang, J.C. Hanson, J.A. Rodríguez, A. Martínez-Arias, J. Phys. Chem. C 111 (2007) 11026.
[48] G.K. Boreskov, Adv. Catal. 15 (1964) 285.
[49] Y. Madier, C. Descorme, A.M. Le Govic, D. Duprez, J. Phys. Chem. B 103 (1999) 10999.
[50] A.B. Hungría, A. Martínez-Arias, M. Fernández-García, A. Iglesias-Juez, A. Guerrero-Ruiz, J.J. Calvino, J.C. Conesa, J. Soria, Chem. Mater. 15 (2003) 4309.
[51] C.T. Au, Y.H. Hu, H.L. Wan, Catal. Lett. 36 (1996) 159.
[52] L. Kundakovic, M. Flytzani-Stephanopoulos, J. Catal. 179 (1998) 203.
[53] C.T. Au, Y.H. Hu, H.L. Wan, Catal. Lett. 27 (1994) 199.
[54] L. de Rogatis, T. Montini, A. Cognigni, L. Olivi, P. Fornasiero, Catal. Today 145 (2009) 176.
[55] Y. Okamoto, T. Kubota, H. Gotoh, Y. Ohto, H. Aritani, T. Tanaka, S. Yoshida, J. Chem. Soc. Faraday Trans. 94 (1998) 3743.
[56] A. Caballero, J.J. Morales, A.M. Cordón, J.P. Holgado, J.P. Espinós, A.R. González-Elipe, J. Catal. 235 (2005) 295.
[57] K. Otsuka, Y. Wang, E. Sunada, I. Yamanaka, J. Catal. 175 (1998) 152.
[58] A. Martínez-Arias, A.B. Hungría, M. Fernández-García, J.C. Conesa, G. Munuera, J. Phys. Chem. B 108 (2004) 17983.
[59] L. Durivault, O. Brylev, D. Reyter, M. Sarrazin, D. Bélanger, L. Roué, J. Alloys Compd. 432 (2007) 323.
[60] F. Tuinstra, J.L. Koenig, J. Chem. Phys. 53 (1970) 1126.
[61] R.P. Bidano, D.B. Fischbachl, Solid State Commun. 39 (1981) 341.